Efficient Solution Algorithms for the Riemann Problem for Real Gases*

PHILLIP COLELLA

*Lawrence Berkeley Laboratory, University of California,
Berkeley, California 94720*

AND

HARLAND M. GLAZ

*Applied Mathematics Branch, Naval Surface Weapons Center,
White Oak, Silver Spring, Maryland 20910*

A procedure for constructing solutions to the Riemann problem for gas dynamics with a general convex equation of state is given. Approximate procedures, involving a local parametrization of the equation of state, are introduced in order to calculate numerical fluxes in conservative finite difference schemes. This leads to difference schemes which are as accurate and almost as fast as the analogous schemes for polytropic gases. Numerical results in one and two space variables are presented. © 1985 Academic Press, Inc.

0. INTRODUCTION

The solution of the Riemann problem in the context of the numerical solution of the equations of inviscid compressible flow is considered here. The conservation form of these equations in one Cartesian space variable is

$$\frac{\partial U}{\partial t} + \frac{\partial F(U)}{\partial x} = 0. \tag{1}$$

The Riemann problem is the initial value problem for (1) with initial data

$$U(x, 0) = \begin{cases} U_L, & x < 0, \\ U_R, & x > 0. \end{cases} \tag{2}$$

264

The solution is a function of the similarity variable $\xi = x/t$ and consists of four constant states separated by elementary waves.

With the exception of the random choice method, numerical schemes for solving (1) which utilize the Riemann problem do not make use of all of the information which is available in the exact solution. This is due to averaging operations which are a part of such schemes. Therefore, one would like to extract, as efficiently as possible, those pieces of information which are actually used.

The goal of this work is the development of approximate solution algorithms for the Riemann problem for (1) with a general convex equation of state (EOS) which can be used in multidimensional calculations with the second order Godunov methods such as those described in [3, 6, 22, 24]. The requirements for such an algorithm are that it be almost as efficient as the corresponding polytropic algorithms, that it be sufficiently accurate to maintain the high-order accuracy of the underlying finite difference scheme in smooth flow, and that it correctly resolves strong wave interactions. The main difficulty encountered in this program is the avoidance of multiple equation of state evaluations. To overcome this problem, a local parametrization of the equation of state is constructed, and the jump conditions for this parameter are derived. The same formulation is used for smooth and nonsmooth flow. Furthermore, no new iterations are required by the introduction of these parameters.

In considering this problem, we shall restrict our attention to a specific Riemann problem solver for use in unsteady gas dynamics. However, the techniques used here can be applied in other situations, such as for the Riemann problems arising in upwind algorithms for steady supersonic flow [13]. These techniques can also be applied to the approximate Riemann solvers of the type considered by Roe [19, 4].

The special case of a polytropic equation of state has been treated extensively in the literature. The main developments have concerned numerical iteration schemes in the pressure-particle velocity plane to determine the strengths of the two nonlinear waves. Godunov [14] introduced a fixed point iteration which was later improved substantially by Chorin [1]. It was noted by van Leer [22] that very little extra work is involved in implementing a Newton iteration which, of course, has a higher convergence rate. Colella [3] used the Newton approach but made the modification (applicable to other iteration schemes as well) that the rarefaction jump formulas can be replaced by the simpler shock jump formulas in the phase space iteration with only a small loss of accuracy. The current situation is that robust, very efficient, and vectorizable methods exist for this special case; in particular, the number of iteration steps can be set to one or two for virtually any problem. Implemented in high-order conservative finite difference schemes, the Riemann problem solver requires only a modest percentage of the total computational effort.

The paper is divided into four sections. In Section 1, the equations of gas dynamics and the associated Riemann problem are described. The exact solution to this problem is presented in detail along with numerical techniques for obtaining this exact solution. These techniques require numerous equation of state

evaluations and are, therefore, prohibitively expensive for use in a finite difference calculation. In Section 2, our local model is introduced and is applied in the construction of a Riemann problem solver which satisfies our requirements; the implementation of the new procedure in a second order Godunov scheme is also outlined. In Section 3, numerical results are presented which validate the approximate Riemann problem solver on a test problem and which demonstrate the power of the overall scheme when applied to a difficult multidimensional problem with real gas effects. Our conclusions are presented in Section 4.

Portions of this work have appeared in preliminary form in [5].

1. Exact Solution of the Riemann Problem

The conserved quantities U and fluxes F in the system of conservation laws (1) are

$$U = \begin{pmatrix} \rho \\ \rho u \\ \rho E \end{pmatrix}, \qquad F = \begin{pmatrix} \rho u \\ \rho u^2 + p \\ \rho E u + p u \end{pmatrix}. \tag{3}$$

Here, ρ is the density, $E = e + \frac{1}{2}u^2$ is the total energy per unit mass, e is the internal energy per unit mass, and u is the velocity. The pressure p is derived from these quantities via an equation of state which we assume to be of the form

$$p \equiv p(\tau, e) \tag{4}$$

where $\tau = \rho^{-1}$ is the specific volume. The function $p(\cdot, \cdot)$ will be assumed to satisfy conditions which ensure that the system (1) is hyperbolic and that the Riemann problem (2) always possesses a unique solution. The inequalities $p_\tau < 0$, $p_e > 0$ are sufficient [17] but not necessary [20] for this purpose.

The characteristic speeds for (1), i.e., the eigenvalues of the Jacobian matrix $\nabla_U F$, are $\lambda^{\pm,0} = u \pm c, u$ where the sound speed c is defined by

$$c^2 = \tau^2(p p_e - p_\tau). \tag{5}$$

This formula exhibits the wave speeds as functions of state, and an explicit isentropic law is not required for their determination. However, an equivalent definition [17] is $c^2 \equiv \partial p/\partial \rho|_S$, where S is the entropy. To ensure that the only elementary hydrodynamic waves we need to consider in the Riemann problem are either shocks or rarefactions, we restrict our attention to equations of state that are convex, i.e., $\partial^2 p/\partial \rho^2|_S > 0$.

The Lagrangian sound speed is defined by

$$C \equiv \rho c. \tag{6}$$

In analogy with the special case of a polytropic gas, we define a dimensionless "isentropic Γ":

$$\Gamma(\tau, e) \equiv \frac{C^2}{p\rho}. \tag{7}$$

Another dimensionless quantity is

$$\gamma(\tau, e) \equiv \frac{p\tau}{e} + 1. \tag{8}$$

For polytropic gases, γ is the ratio of specific heats and $\gamma = \Gamma$. Neither statement is true in general.

We also need Eqs. (1) expressed in nonconservation form

$$V_t + A(V)\, V_x = 0 \tag{9}$$

where

$$V = \begin{pmatrix} \tau \\ u \\ p \end{pmatrix}, \qquad A(V) = \begin{pmatrix} u & -\tau & 0 \\ 0 & u & \tau \\ 0 & \rho c^2 & u \end{pmatrix}. \tag{10}$$

The systems (1) and (9) are equivalent for smooth flow. The matrix A has left and right eigenvectors (l^+, r^+), (l^-, r^-), and (l^0, r^0) associated with the eigenvalues $\lambda^{\pm,0}$ defined above. If these vectors are suitably normalized, it can be shown that they are biorthonormal, i.e., $l^\alpha \cdot r^\beta = \delta_{\alpha\beta}$. The characteristic equations for (9) are obtained by setting $l \cdot dV = 0$ for $l = l^{\pm,0}$:

$$l^+ \cdot dV = C^{-1}\, dp + du = 0$$

$$l^- \cdot dV = C^{-1}\, dp - du = 0 \tag{11}$$

$$l^0 \cdot dV = C^{-2}\, dp + d\tau = 0.$$

These relations hold along characteristic curves in physical space given by $dx/dt = \lambda^{\pm,0}$, as well as in V (phase) space.

The solution of the Riemann problem (1), (2) is illustrated in Fig. 1 for shock tube initial data. The backward facing wave (U_{*L}, U_L) and the forward facing wave (U_{*R}, U_R) may be either shock waves or rarefaction waves for general initial data. The center wave (U_{*L}, U_{*R}) must be a contact discontinuity across which there is no pressure or velocity jump. The exact wave structure cannot be uniquely determined by the jump conditions alone, and an entropy condition must be added. Note that a rarefaction wave has finite extent in ξ-space whereas a shock wave is infinitely thin.

In Fig. 2, the problem is presented in the pressure-particle velocity plane; the case shown corresponds to Fig. 1. The two curves consist of those states which can be
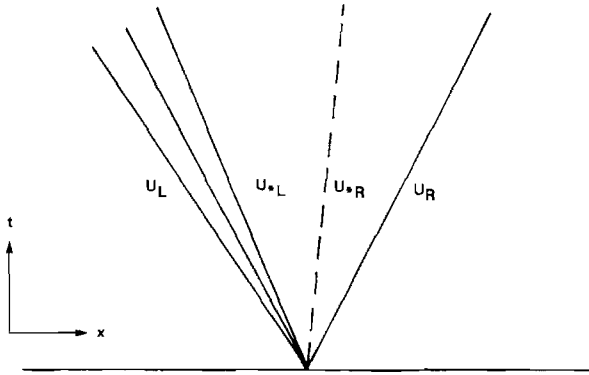
FIG. 1. The solution of the Riemann problem in physical space.

connected on the right to U_L and on the left to U_R by elementary nonlinear waves (i.e., shock waves or rarefaction waves) satisfying the entropy condition. For further details on Riemann problems and such diagrams, see [7]. We now consider the structure of the shock and rarefaction curves in the p–u plane.

The shock curves are determined by the Rankine–Hugoniot conditions,

$$[u] = \pm \frac{[p]}{W}$$

$$\frac{[p]}{W^2} = -[\tau] \tag{12}$$
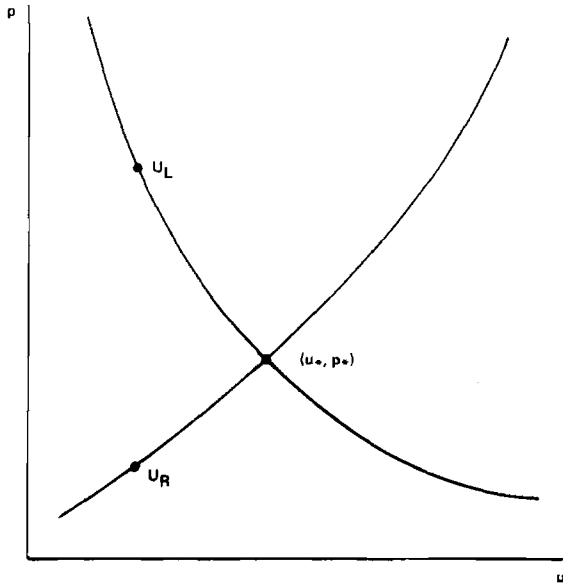
$$[e] = -\bar{p}[\tau].$$

FIG. 2. Wave curves and solution of the Riemann problem in the pressure-particle velocity plane.

Here, $[q] \equiv q_* - q_S$ denotes the jump in q across a wave, $S = L, R, \bar{q} = \frac{1}{2}(q_* + q_S)$, and W is the Lagrangian wave speed or mass flux crossing the wave. The interpretation of W as a slope in the p–u plane is quite useful. The first two equations in (12) are equivalent to conservation of mass and momentum and the third equation is conservation of energy. The choice of sign is positive (negative) for forward (backward) facing shocks. Given U_S and p_*, the jump conditions (12) and the equation of state uniquely determine the postshock state U_*.

The rarefaction curves may be defined as the projection onto the p–u plane of the integral curves of $r^\pm$ in V-space. It follows from our assumptions on the equation of state that the pressure is monotone across a rarefaction wave. Therefore, the equations may be taken to be

$$dr/dp = -C^{-2}$$
$$du/dp = \pm C^{-1}. \tag{13}$$

The first of these equations is the isentropic law, and the second states that the appropriate Riemann invariant is constant across the wave. For the special case of a centered wave (as illustrated in Fig. 1), the additional equation

$$\xi \equiv x/t = u \pm c \tag{14}$$

holds because $\xi = $ constant lines are $\lambda^\pm$-characteristics.

The main step in solving the Riemann problem is the computation of the pair (p_*, u_*) which is the unique intersection point of the two wave curves through U_L and U_R in the p–u plane. The solution cannot be obtained in closed form, even for a polytropic gas, and a numerical iteration is required; the details of this procedure will be described below. We remark here that the wave curves are C^∞ except at $U_{L,R}$, where they are C^2 [7]. Thus, the standard numerical techniques for determining the intersection of two plane curves can be expected to converge at their design rates.

The second part of the procedure is to calculate the solution at some given point ξ. Let $\chi = \text{sgn}(\xi - u_*)$ and define

$$(U_S, W_S, c_S) = \begin{cases} (U_L, W_L, c_L) & \text{if } \chi = -1, \\ (U_R, W_R, c_R) & \text{if } \chi = 1; \end{cases}$$

$$\hat{u}_S = \chi u_S, \qquad \hat{\xi} = \chi \xi, \qquad \hat{u}_* = \chi u_*.$$

In case $p_* > p_S$, so that the wave is a shock, the second jump condition (12) implies that

$$\rho_* = \left(\rho_S^{-1} - \frac{(p_* - p_S)}{W_S^2} \right)^{-1}. \tag{15}$$

The sound speed c_* is then computed from the third jump condition and (7). In case $p_* < p_S$, so that the wave is a rarefaction, the ordinary differential equations

(13) are solved with initial data $U = U_S$ to the final point $p = p_*$. This yields ρ_* from which c_* may be calculated using the equation of state. Then define

$$
\hat{\lambda}_S, \hat{\lambda}_* = \begin{cases} \hat{u}_S + c_S, \hat{u}_* + c_* & \text{if } p_* < p_S, \\[2ex] \hat{u}_S + \dfrac{W_S}{\rho_S} & \text{if } p_* > p_S. \end{cases}
$$

We then evaluate p, ρ, u at ξ as follows:

$$
p, \rho, u = \begin{cases} p_*, \rho_*, u_* & \text{if } \hat{\xi} \leqslant \hat{\lambda}_* \\ p_S, \rho_S, u_S & \text{if } \hat{\xi} > \hat{\lambda}_S. \end{cases}
$$

If $\hat{\lambda}_S > \hat{\xi} > \hat{\lambda}_*$, then the solution is being evaluated inside a rarefaction fan. In this case, the system (13) is solved with initial data $U = U_S$ to the final point $\hat{u} + c = \hat{\xi}$. Our assumptions on the equation of state are sufficient to guarantee the existence and uniqueness of such a point.

We now present the details of the iteration schemes for determining (u_*, p_*) given U_L and U_R. For either a shock or rarefaction wave, the postwave state is uniquely determined by the prewave state and p_*. In particular, we can define u_{*S}, the postwave velocity as a function of p_* and U_S, $S = L, R$. We can also define the mean Lagrangian wave speeds

$$
W_S = \begin{cases} \dfrac{|p_* - p_S|}{|u_{*S} - u_S|} & \text{if } u_{*S} \neq u_S \\[2ex] C_S & \text{if } u_{*S} = u_S. \end{cases} \tag{16}
$$

In the case of a shock, W_S is the quantity which appears in the Rankine–Hugoniot conditions (12). In either case, $W_S \equiv W_S(p_*; U_S)$.

At the solution, $u_{*L} = u_{*R} = u_*$. We will describe the secant method and Newton's method for the equation

$$
u_{*L}(p_*) - u_{*R}(p_*) = 0. \tag{17}
$$

At each step of either of these iteration schemes, it is necessary to obtain values for $W_{L,R}$ given the current iterate of p_*. This involves an inner iteration loop which we outline at the end of the section.

The secant method applied to the function (17) becomes

$$
u_{*S}^\nu = u_S \pm \frac{p_*^\nu - p_S}{W_S^\nu}
$$

$$
p_*^{\nu+1} = p_*^\nu - (u_{*R}^\nu - u_{*L}^\nu) \cdot \left[\frac{|p_*^\nu - p_*^{\nu-1}|}{|u_{*L}^\nu - u_{*L}^{\nu-1}| + |u_{*R}^\nu - u_{*R}^{\nu-1}|} \right] \tag{18}
$$

for $v = 1, 2,...$. Here, and in what follows, the combination of $(S, \pm)$ are to be taken as either $(L, -)$ or $(R, +)$. The first two guesses used to start the iteration are obtained using Godunov's iteration scheme [14, 1].

Our derivation of a Newton iteration follows van Leer [22]. Applying Newton's method to (17) yields

$$u^v_{*S} = u_S \pm \frac{p^v_* - p_S}{W^v_S}$$

$$p^{v+1}_* = p^v_* - \frac{Z_L Z_R (u_{*R} - u_{*L})}{Z_L + Z_R} \tag{19}$$

for $v = 0, 1, 2,...$, where $Z_S = |dp_*/du_{*S}|$. For a polytropic gas, Z_S can be obtained in closed form as a function of U_S and the current iterate of p_* [22]. Along the rarefaction curve, $|dp_*/du_{*S}|$ is given by integrating (13):

$$\left|\frac{dp_*}{du_{*S}}\right| = C(p_*, \rho_*).$$

The derivation for the shock curves is somewhat more involved. We begin by noting that

$$\left|\frac{dp_*}{du_*}\right| = \frac{W^2}{W - (dW/dp_*)[p]} \tag{20}$$

where the subscript S has been dropped for convenience. Equation (20) follows from the first jump condition (12). Since W is known, this reduces the problem to calculating dW/dp_* or, equivalently, dW^2/dp_*. Noting that $e_p = p_e^{-1}$ and $e_\tau = -p_\tau/p_e$, we compute

$$\frac{de_*}{dp_*} = \frac{d}{dp_*} e(p_*, \tau_*)$$

$$= \frac{d}{dp_*} e\left(p_*, \tau - \frac{[p]}{W^2}\right)$$

$$= p_e^{-1} - \frac{p_\tau}{p_e}\left(-W^{-2} + [p] W^{-4} \frac{dW^2}{dp_*}\right). \tag{21}$$

Differentiating $\frac{1}{2}[p^2] = W^2[e]$ which follows from (12) and substituting (21), we obtain

$$p_* = W^2 \frac{de_*}{dp_*} + [e] \frac{dW^2}{dp_*}$$

$$= \left[p_e^{-1} + \frac{p_\tau}{pe}\left(W^{-2} - [p] W^{-4} \frac{dW^2}{dp_*}\right)\right] W^2 + \frac{dW^2}{dp_*} [e]. \tag{22}$$

Multiplying both sides of (22) by p_e, rearranging terms, and using (5), we obtain

$$\frac{dW^2}{dp_*} = \frac{(C_*^2 - W^2)\, W^2}{(\bar{p}p_e - p_\tau)[p]}, \tag{23}$$

where the derivatives of p are evaluated at (p_*, τ_*). Upon substitution of (23) into (20), we obtain a formula for $Z(p_*; U)$ in closed form.

There are several reasons for preferring the secant iteration to the Newton iteration in practice. Most important, the thermodynamic derivatives p_e and p_τ often are not available in real gas equation of state software. If they are available, their accurate computation requires extra work, partially offsetting the gain in convergence rate.

We now consider the problem of determining $W(p_*; U)$. For the jump across a simple wave, this is trivial because u_* is obtained directly from the integration of (13) across the wave. Across a shock wave, we have $W^2[e] = \frac{1}{2}[p^2]$. Now,

$$e_* = e(p_*, \tau_*)$$

$$= e\left(p_*, \tau - \frac{[p]}{W^2}\right).$$

Combining these two relations, one obtains a single nonlinear equation in the single unknown W^2 which can be solved by any standard numerical procedure.

In the event that γ_* is somehow known a priori, the inner iteration for W^2 across a shock wave can be eliminated. Indeed, it follows easily that

$$W^2 = \frac{1}{2}\,(p_*^2 - p^2)\Big/\left[\frac{p_*}{\gamma_* - 1}\left(\tau - \frac{p_* - p}{W^2}\right) - e\right]. \tag{24}$$

In this case, Eq. (24) can be solved for W^2 in closed form.

The algorithms developed in this section all involve equation of state evaluations inside the iteration loop. Our strategy to avoid this, described in the next section, is to obtain an approximate formula for $\gamma_* = \gamma_*(p_*; U)$ in closed form and use (24) and the secant iteration (18); alternatively, the Newton algorithm can be similarly adapted if the appropriate equation of state derivatives are available. It is also essential to avoid numerical integrations of (13) because an equation of state evaluation is required at each step of the ODE integration.

2. LOCAL MODELS FOR THE EQUATION OF STATE AND THE APPROXIMATE SOLUTION TO THE RIEMANN PROBLEM

In using Godunov's method or any of its second order extensions, the solution of the Riemann problem must be calculated one or more times per mesh point per

dimension per time step. The exact algorithms of the preceding section require numerous evaluations of the equation of state and therefore do not lead to solution algorithms for the equations of gas dynamics which are cost competitive with conventional finite difference methods. In this section, we present a method for obtaining an approximate solution to the Riemann problem which is based on a local model for the equation of state. The resulting numerical methods require only one evaluation of the pressure per mesh point per dimension per time step. In addition, the quantity Γ defined by (7) must also be supplied by the equation of state.

Our model is based on the idea of expressing the equation of state in terms of γ, defined by (8). For the purpose of computing numerical fluxes, γ will be treated as a separate dependent variable; the solution of characteristic equations and Riemann problems will necessarily involve an approximate computation of the jump in γ across such waves.

Given the crudeness of some of the approximations, our model leads to a surprisingly effective numerical procedure for nonpolytropic gases. One reason for this is that γ is a slowly varying function of the thermodynamic variables for real gases: although p, ρ, e may vary over many orders of magnitude, γ stays in the range $1 < \gamma \leqslant \frac{5}{3}$. Another reason is that, given a prejump state, the postjump pressure, and a postjump γ, the Rankine–Hugoniot conditions for the jump can be solved exactly at essentially the same cost as in the polytropic case.

In the event that γ is not a slowly varying state function, such as in the case of compressible water, a different local model corresponding to a different parametrization of the equation of state might be required; however, the principles of its construction would remain the same. Our treatment here is restricted to models based on γ. We remark that we have performed successful computations using this model for problems where γ changes by more than an order of magnitude across the shock.

We now consider the dynamic behavior of γ. Since γ is a function of the thermodynamic state of the fluid, it is natural to consider its dynamics along the streamline characteristic, which we parametrize by σ_0. By definition,

$$\frac{d\gamma}{d\sigma_0} = \frac{\partial \gamma}{\partial \tau} \frac{d\tau}{d\sigma_0} + \frac{\partial \gamma}{\partial e} \frac{de}{d\sigma_0}. \tag{25}$$

Using (5), (7), (8), and the first law of thermodynamics, this becomes

$$\frac{d\gamma}{d\sigma_0} = \left(1 - \frac{\gamma}{\Gamma}\right) (\gamma - 1) \frac{1}{p} \frac{dp}{d\sigma_0}. \tag{26}$$

Thus, the calculation of the dynamics of γ in smooth flow does not require the total derivative of p with respect to (τ, e); the only information about these derivatives that is required is contained in Γ.

In general, it is not possible to specify how γ behaves across a discontinuity without solving the full Rankine–Hugoniot conditions. However, if the jump is not

too large, then the jump conditions for γ are well-approximated by an integrated form of the characteristic equation (26), since the Hugoniot curve and the rarefaction curve have second order contact at U_0,

$$\gamma_* - \gamma_0 = \left(1 - \frac{\bar{\gamma}}{\bar{\Gamma}}\right)(\bar{\gamma} - 1)\frac{1}{\bar{p}}(p_* - p_0) + O(p_* - p_0)^3 \tag{27}$$

where $\bar{\gamma}$, $\bar{\Gamma}$, $\bar{p}$ are suitably centered across the jump. The relations (26), (27) will be used to calculate the local dynamics of γ in our scheme.

The above local model leads to the following approximate solution to the Riemann problem. Suppose that we are given left and right states $(U_L, \gamma_L, \Gamma_L)$ and $(U_R, \gamma_R, \Gamma_R)$. We follow the general procedure of the preceding sections to calculate the approximate value of the similarity solution at any point $\xi = x/t$. We use the secant iteration scheme (18) to determine (u_*, p_*) except that the exact values of W_S at each iterate are replaced by approximate ones based on (27). Specifically, given p_* from the main iteration, we define $W \equiv W(p_*; U_S, \gamma_S, \Gamma_S)$ to be the solution to the equation

$$W^2(e_{*S} - e_S) = \tfrac{1}{2}(p_*^2 - p_S^2) \tag{28}$$

where

$$e_{*S} = \frac{p_* \tau_*}{\gamma_{*S} - 1} = \frac{p_*}{\gamma_{*S} - 1}\left(\tau_S - \frac{p_* - p_S}{W^2}\right), \tag{29}$$

$$e_S = \frac{p_S \tau_S}{\gamma_S - 1}, \tag{30}$$

$$\hat{\gamma}_{*S} = \gamma_S + \left(1 - \frac{\bar{\gamma}}{\bar{\Gamma}}\right)(\bar{\gamma} - 1)\frac{p_* - p_S}{(\tfrac{1}{2})(p_* + p_S)}; \tag{31}$$

$$\gamma_{*S} = \max(\gamma_{\min}, \min(\hat{\gamma}_{*S}, \gamma_{\max})), \tag{32}$$

$$\bar{\gamma} = \tfrac{1}{2}(\gamma_L + \gamma_R), \qquad \bar{\Gamma} = \tfrac{1}{2}(\Gamma_L + \Gamma_R), \tag{33}$$

and $\gamma_{\min}$, $\gamma_{\max}$ are limiting values for γ which might, for example, be set by taking the max and min of γ over several neighboring grid points in a finite difference calculation. As noted in the discussion of (24), Eqs. (28), (29) are easily solved to give an explicit expression for W^2,

$$W^2 = (p_* - p_S)\left(p_* + \frac{1}{2}(\gamma_{*S} - 1)(p_* + p_S)\right)\bigg/\left(p_* \tau_S - \frac{\gamma_{*S} - 1}{\gamma_S - 1}p_S \tau_S\right). \tag{34}$$

This expression is exact in the case of a polytropic equation of state. Also, taking the limit $U_L - U_R \to 0$, we obtain

$$W^2 = \Gamma_S p_S \rho_S + O(U_L - U_R) \tag{35}$$

so that the values obtained for (u_*, p_*) in the weak wave limit are correct to second order in the jumps.

The shock jump formula (28) is used to compute W^2 even for rarefaction waves. Since the shock and rarefaction curves through U_S have second order contact at U_S, the error introduced can be expected to be of higher order than a second-order accurate finite difference scheme's overall truncation error. Also, strong expansion waves tend to spread out over several zones, thereby making the computation of a strong rarefaction jump an extremely rare occurrence in a finite difference computation.

The evaluation of the solution at a given point $\xi = x/t$ proceeds as in Section 2 with one difference: if ξ is located inside a rarefaction fan, then linear interpolation between the pre- and postwave states is used to determine the desired value. This approximates the exact procedure of integrating (13) through the fan until ξ is reached. The value of $\gamma(\xi)$ inside a fan is also obtained by linear interpolation, although an approximate form of (26) could be used once $p(\xi)$ is known. It is easy to check that the values of p, u, ρ, γ obtained using this algorithm are correct to second order in the jump. This level of accuracy is sufficient to imply that a Godunov-type scheme which is second order accurate in smooth flow remains so if the exact Riemann problem solver is replaced by our approximate Riemann problem solver.

To illustrate how our Riemann problem solver is implemented in a finite difference scheme, we describe the extension of the scheme for a polytropic gas introduced in [6] to the case of a real gas. We restrict attention to the case of a single space dimension, Cartesian symmetry, and no source terms; the extension to the other situations as described in [6] are straightforward. Also, the dissipation mechanisms discussed in [6] and [24] are required for the corresponding real gas algorithms, and can be applied without modification. We denote by $x_{j+1/2}$ the boundary between the jth and $(j+1)$th zones, and define $\Delta x_j = x_{j+1/2} - x_{j-1/2}$, $x_j = \frac{1}{2}(x_{j+1/2} + x_{j-1/2})$. We assume that, at time t^n, we know U_j^n, an approximation to the average of the solution to (1) across the jth zone:

$$U_j^n = (1/\Delta x_j) \int_{x_{j-1/2}}^{x_{j+1/2}} U(x, t^n)\, dx.$$

We wish to calculate U_j^{n+1}, the approximate solution at time $t^{n+1} = t^n + \Delta t$. In outline, the second order Godunov algorithms for doing so consist of four steps:

(1) the calculation of interpolated profiles for the dependent variables (not necessarily the conserved quantities);

(2) the construction of time-centered left and right states $V_{j+1/2,L}^{n+1/2}$, $V_{j+1/2,R}^{n+1/2}$ at $x_{j+1/2}$;

(3) the solution of the Riemann problem at $x_{j+1/2}$ with left and right states constructed as in (2), to give $V_{j+1/2}^{n+1/2}$; and

(4)   the conservative differencing of the fluxes $F_{j+1/2} = F(U(V_{j+1/2}^{n+1/2}))$,

$$U_j^{n+1} = U_j^n + \frac{\Delta t}{\Delta x_j} (F_{j-1/2} - F_{j+1/2}).$$

We consider first the equations of Lagrangian hydrodynamics, i. e., equations of the form (1) with

$$U = \begin{pmatrix} \tau \\ u \\ E \end{pmatrix}, \qquad F = \begin{pmatrix} -u \\ p \\ up \end{pmatrix}, \tag{36}$$

and where the mass coordinate m is used in place of x in (1). We begin by using the equation of state to obtain $p_j^n = p(\tau_j^n, E_j^n - \frac{1}{2}(u_j^n)^2)$, $C_j^n = C(\tau_j^n, E_j^n - \frac{1}{2}(u_j^n)^2)$. We then calculate

$$\gamma_j^n = \frac{p_j^n}{\rho_j^n e_j^n} + 1, \qquad \Gamma_j^n = \frac{\tau_j^n (C_j^n)^2}{p_j^n}. \tag{37}$$

We then interpolate the variables p, u, τ as functions of m using either the piecewise parabolic algorithm described in [6], or the piecewise linear algorithm described in [22, 3]. Interpolants are not constructed for γ or Γ.

The left and right states at $m_{j+1/2}$ are constructed by averaging $p, u,$ and τ over the domains of dependence of the point $(m_{j+1/2}, t^{n+1})$ to the left and right of $m_{j+1/2}$:

$$a_{j+1/2,L} = (C_j^n \Delta t)^{-1} \int_{m_{j+1/2} - C_j^n \Delta t}^{m_{j+1/2}} a(m) \, dm$$

$$a_{j+1/2,R} = (C_{j+1}^n \Delta t)^{-1} \int_{m_{j+1/2}}^{m_{j+1/2} + C_{j+1}^n \Delta t} a(m) \, dm \tag{38}$$

for $a = p, u, \tau$, and

$$\gamma_{j+1/2,L} = \gamma_j, \qquad \Gamma_{j+1/2,L} = \Gamma_j,$$

$$\gamma_{j+1/2,R} = \gamma_{j+1}, \qquad \Gamma_{j+1/2,R} = \Gamma_{j+1}. \tag{39}$$

The approximate solution to the Riemann problem is then computed with the left and right states given by (38), (39). Only the iteration procedure is performed because only the central pressure $p_{*j+1/2}$ and velocity $u_{*j+1/2}$ is required to calculate the fluxes.

The final conservative difference step is given by

$$\tau_j^{n+1} = \tau_j^n - \frac{\Delta t}{\Delta m_j} (u_{*j-1/2} - u_{*j+1/2})$$

$$u_j^{n+1} = u_j^n + \frac{\Delta t}{\Delta m_j} (p_{*j-1/2} - p_{*j+1/2}) \tag{40}$$

$$E_j^{n+1} = E_j^n + \frac{\Delta t}{\Delta m_j} (p_{*j-1/2} u_{*j-1/2} - p_{*j+1/2} u_{*j+1/2}).$$

In smooth flow, the scheme described here is second order accurate. Superficially, this appears to be incorrect since the piecewise constant interpolation of γ is only first order. This is sufficient for the purpose of computing second order accurate fluxes because these fluxes involve only pressures and velocities. This can be seen quantitatively using the relation (35) adapted to Lagrangian hydrodynamics:

$$W_{j+1/2,S} = \left(\frac{\Gamma_{j+1/2,S}\, p_{j+1/2,S}}{\tau_{j+1/2,S}}\right)^{1/2} + O(U_{j+1} - U_j), \qquad S = \text{L, R}. \qquad (41)$$

This is sufficient to imply that $(u_{*j+1/2}, p_{*j+1/2})$ is correct except for errors $O((U_{j+1} - U_j)^2)$ in smooth flow, and this is in turn sufficient to guarantee second order accuracy of the overall method. Unfortunately, this simplification disappears for the single-step Eulerian algorithm discussed below; a value for γ is required to compute the energy flux, so that γ must be interpolated to preserve second order accuracy.

The extension of the single step Eulerian scheme for solving (1), (3) described in Section 3 of [6] is equally straightforward, following the outline given above. Since this algorithm is used to obtain the computational results presented in the next section, we take some care to describe it in detail.

This algorithm, like the Lagrangian algorithm, consists of the four steps given above. In the interpolation step, we calculate profiles of the quantities $q = p, \rho, u, \gamma$, given $q_j^n = q(U_j^n)$, subject to monotonicity constraints. As before, one can use piecewise linear interpolation or piecewise quadratic interpolation. In the results obtained below, we used the piecewise linear formulae, so that

$$q(x) = q_j^n + \left(\frac{x - x_j}{\Delta x_j}\right) \Delta q_j^n, \qquad x_{j-1/2} < x < x_{j+1/2},$$

where Δq_j is calculated using the algorithm described in [3]. In regions where the solution is smooth, $\Delta q_j / \Delta x_j$ is a fourth-order central difference approximation to $\partial q/\partial x|_{x_j}$.

To obtain our left and right states, we use our interpolation functions and the nonconservative form of the differential equation (9) to extrapolate left and right limiting values at time $t^n + (\Delta t/2)$,

$$V_{j+1/2,L}^{n+1/2} \approx V_j^n + \frac{\Delta t}{2}\frac{\partial V}{\partial t} + \frac{\Delta x_j}{2}\frac{\partial V}{\partial x} = V_j^n + \left(\frac{\Delta x_j}{2} - \frac{\Delta t}{2}A_j\right)\left(\frac{\partial V}{\partial x}\right)_{x_j}$$

$$V_{j+1/2,R}^{n+1/2} \approx V_{j+1}^n - \left(\frac{\Delta x_{j+1}}{2} + \frac{\Delta t}{2}A_{j+1}\right)\left(\frac{\partial V}{\partial x}\right)_{x_{j+1}}, \qquad (42)$$

where $A_j = A(V_j^n)$.

If we replace $(\partial V/\partial x)$ by $\Delta V_j/\Delta x_j$, where the ΔV_j's were obtained from the slopes calculated in the interpolation step, then this is essentially the algorithm used in smooth regions. In that case, the states $V_{j+1/2,L}^{n+1/2}$, $V_{j+1/2,R}^{n+1/2}$, are constructed such that

$V_{j+1/2}^{n+1/2}$ is an approximation to a solution to the characteristic form of the equations at $(x_{j+1/2}, t^n + (\Delta t/2))$, up to terms of second order, so that the algorithm is second order in space and time. However, we make several modifications to (42), which have an effect only at discontinuities. We do not include all the corrections to V_j^n, V_{j+1}^n, given by (42), but only those components in an expansion in terms of the right eigenvectors of A corresponding to waves approaching $x_{j+1/2}$. We also take advantage of the fact that increments of the solution propagate along characteristics, so that the reference state against which we measure those increments is, within limits, arbitrary. We obtain, then

$$V_{j+1/2,L}^{n+1/2} = \tilde{V}_L + P_>(V_j^n - \tilde{V}_L) + P_> \left(\frac{\Delta x_j}{2} - \frac{\Delta t}{2} A_j \right) \left(\frac{\Delta V_j}{\Delta x_j} \right)$$

$$V_{j+1/2,R}^{n+1/2} = \tilde{V}_R + P_<(V_{j+1}^n - \tilde{V}_R) - P_< \left(\frac{\Delta x_{j+1}}{2} + \frac{\Delta t}{2} A_{j+1} \right) \left(\frac{\Delta V_{j+1}}{\Delta x_{j+1}} \right),$$

(43)

where the operators $P_>$, $P_<$ are defined by

$$P_> w = \sum_{\lambda_j^\# > 0} (l_j^\# \cdot w) r_j^\#,$$

$$P_< w = \sum_{\lambda_{j+1}^\# < 0} (l_{j+1}^\# \cdot w) r_{j+1}^\#.$$

Here, and in what follows, we take expressions involving $\#$ to mean $\#$ ranging over $+, -, 0$.

The reference states $\tilde{V}_L$, $\tilde{V}_R$ are chosen so as to reduce, to as great an extent as possible, the degree to which we rely on the linearized equations in calculating $V_{j+1/2,L}^{n+1/2}$, $V_{j+1/2,R}^{n+1/2}$. For example, if we take

$$\tilde{V}_L = V_j^n + \left(\frac{\Delta x_j}{2} - \max(\lambda_j^+, 0) \frac{\Delta t}{2} \right) \left(\frac{\Delta V_j}{\Delta x_j} \right)$$

$$\tilde{V}_R = V_{j+1}^n - \left(\frac{\Delta x_{j+1}}{2} + \min(\lambda_{j+1}^-, 0) \frac{\Delta t}{2} \right) \left(\frac{\Delta V_{j+1}}{\Delta x_{j+1}} \right),$$

(44)

then we eliminate one component of the correction to V_j^n, V_{j+1}^n; in particular, if the flow velocity is zero $V_{j+1/2,L}^{n+1/2} = \tilde{V}_L$, $V_{j+1/2,R}^{n+1/2} = \tilde{V}_R$. Comparing this result with (38), we remark that (38) can be derived starting from the Lagrangian version of (42). Finally, we replace τ, $\Delta \tau$ by expressions involving ρ, $\Delta \rho$, in such a way that, in the absence of p and u gradients, the amount of mass transported across a zone edge is equal to the integral of ρ under the streamline reaching $(x_{j+1/2}, t^{n+1})$. The result, then, is

$$\tilde{q}_L = q_j^n + \frac{1}{2} \left(1 - \frac{\Delta t}{\Delta x_j} (\max(\lambda_j^+, 0)) \right) \Delta q_j, \qquad q = p, \rho, u, v$$

$$\tilde{q}_R = q_{j+1}^n - \frac{1}{2} \left(1 + \frac{\Delta t}{\Delta x_{j+1}} (\min(\lambda_{j+1}^-, 0)) \right) \Delta q_{j+1}$$

$$\beta_L^- = -\left(\Delta u_j - \frac{\Delta p_j}{C_j}\right)\frac{\Delta t}{2\rho_j^n \, \Delta x_j} \qquad \text{if} \quad \lambda_j^- > 0$$

$$= 0 \qquad \text{otherwise,}$$

$$\beta_L^0 = -\left(\frac{\Delta p_j}{C_j^2} - \frac{\Delta \rho_j}{\tilde{\rho}_L \rho_L^0}\right) c_j \frac{\Delta t}{2\Delta x_j} \qquad \text{if} \quad \lambda_j^0 > 0$$

$$= 0 \qquad \text{otherwise,}$$

$$\beta_R^+ = -\left(\Delta u_{j+1} + \frac{\Delta p_{j+1}}{C_{j+1}}\right)\frac{\Delta t}{2\rho_{j+1}^n \, \Delta x_{j+1}} \qquad \text{if} \quad \lambda_{j+1}^+ < 0 \tag{45}$$

$$= 0 \qquad \text{otherwise,}$$

$$\beta_R^0 = \left(\frac{\Delta p_{j+1}}{C_{j+1}^2} - \frac{\Delta \rho_{j+1}}{\tilde{\rho}_R \rho_R^0}\right) c_{j+1} \frac{\Delta t}{2\Delta x_{j+1}} \qquad \text{if} \quad \lambda_{j+1}^0 < 0$$

$$= 0 \qquad \text{otherwise,}$$

where

$$q_L^0 = q_j + \tfrac{1}{2}(1 - (\Delta t/\Delta x_j)\, u_j)\, \Delta q_j,$$

and

$$q_R^0 = q_{j+1}^n - \tfrac{1}{2}(1 + (\Delta t/\Delta x_{j+1})\, u_{j+1})\, \Delta q_{j+1}.$$

Given these expansion coefficients, then

$$V_{j+1/2,L}^{n+1/2} = \tilde{V}_L + \sum \beta_L^\# \, r_j^\#, \quad V_{j+1/2,R}^{n+1/2} = \tilde{V}_R + \sum \beta_R^\# \, r_{j+1}^\#,$$

$$\rho_{j+1/2,L}^{n+1/2} = (\tilde{\rho}_L^{-1} - \beta_L^0 - \beta_L^-)^{-1}$$

$$p_{j+1/2,L}^{n+1/2} = \tilde{p}_L + \beta_L^- C_j^2$$

$$u_{j+1/2,L}^{n+1/2} = \tilde{u}_L - \beta_L^- C_j \tag{46}$$

$$\rho_{j+1/2,R}^{n+1/2} = (\tilde{\rho}_R^{-1} - \beta_R^0 - \beta_R^+)^{-1}$$

$$p_{j+1/2,R}^{n+1/2} = \tilde{p}_R + \beta_R^+ C_{j+1}^2$$

$$u_{j+1/2,R}^{n+1/2} = \tilde{u}_R + \beta_R^+ C_{j+1}.$$

That Eqs. (45), (46) are equivalent to (43), (44) is easily derived, using the identities $P_> \Delta w = \sum_{\lambda^\# > 0} \lambda^\# (l^\# \cdot w) r^\#$, $P_< \Delta w = \sum_{\lambda^\# < 0} \lambda^\# \langle l^\# \cdot w \rangle r^\#$.

Since the above steps are well defined for a general equation of state, we need only define $\gamma_{j+1/2,S}$, $\Gamma_{j+1/2,S}$, $S = L, R$. As in the Lagrangian case, we take $\Gamma_{j+1/2,L} = \Gamma_j$, $\Gamma_{j+1/2,R} = \Gamma_{j+1}$. We take $\gamma_{j+1/2,S}$ to be the value given by the characteristic equation (26) when the velocity has the appropriate sign; otherwise, we use $\tilde{\gamma}_S$,

$$\hat{\gamma}_{j+1/2,L}^{n+1/2} = \gamma_L^0 + 2\left(1 - \frac{\gamma_j}{\Gamma_j}\right)(\gamma_j - 1)\frac{(p_{j+1/2,L}^{n+1/2} - p_L^0)}{(p_{j+1/2,L}^{n+1/2} + p_L^0)} \qquad \text{if} \quad u_j > 0,$$

$$= \tilde{\gamma}_L \qquad \text{otherwise,}$$

$$\hat{\gamma}_{j+1/2,R}^{n+1/2} = \gamma_R^0 + 2\left(1 - \frac{\gamma_{j+1}}{\Gamma_{j+1}}\right)(\gamma_{j+1} - 1)\frac{(p_{j+1/2,R}^{n+1/2} - p_R^0)}{(p_{j+1/2,R}^{n+1/2} + p_R^0)} \qquad \text{if} \quad u_{j+1} < 0,$$

$$= \tilde{\gamma}_R \qquad\qquad\qquad \text{otherwise,}$$

$$\gamma_{j+1/2,S}^{n+1/2} = \max(\gamma_{min}, \min(\gamma_{max}, \hat{\gamma}_{j+1/2,S}^{n+1/2})). \tag{47}$$

Thus we have all the data we need to solve the Riemann problem at $x_{j+1/2}$ using the algorithm described in this section. If we denote by $q_{j+1/2}^{n+1/2}$, $q = p, \rho, u, \gamma$, the values so obtained, the conservative flux $F_{j+1/2}$ is given by

$$F_{j+1/2} = \begin{pmatrix} \rho_{j+1/2}^{n+1/2} u_{j+1/2}^{n+1/2} \\ \rho_{j+1/2}^{n+1/2}(u_{j+1/2}^{n+1/2})^2 + p_{j+1/2}^{n+1/2} \\ \rho_{j+1/2}^{n+1/2} u_{j+1/2}^{n+1/2}\left(\dfrac{(u_{j+1/2}^{n+1/2})^2}{2} + \dfrac{\gamma_{j+1/2}^{n+1/2} p_{j+1/2}^{n+1/2}}{\rho_{j+1/2}^{n+1/2}(\gamma_{j+1/2}^{n+1/2} - 1)}\right) \end{pmatrix}. \tag{48}$$

3. RESULTS

We have implemented the methods described in Section 2 and tested them for a variety of equations of state. The calculations discussed here have been performed with the Eulerian second order Godunov scheme described in the previous section. We shall present the results of two test calculations here: one a simple shock tube in one space variable, the other a complicated shock reflection problem in two space variables, where the real gas EOS has substantial effect on the nature of waves generated. The latter calculation was performed using the standard second order operator splitting technique, with the component one-dimensional algorithm as in Section 2.

The first test problem is a shock tube in one space dimension in Cartesian coordinates. The material to the right of the initial discontinuity is air, initially at atmospheric conditions, the equation of state for which is that given by Gilmore [10]. The material on the left consists of high explosive product gases, the equation of state for which is given by the JWL formula [9, 21]:

$$p = A\left(1 - \frac{\omega}{R_1 V}\right)e^{-R_1 V} + B\left(1 - \frac{\omega}{R_2 V}\right)e^{-R_2 V} + \frac{\omega e}{\tau} \tag{49}$$

where $V = (\tau/\tau_0)$, $\tau_0 = \rho_0^{-1}$ and ρ_0 is a reference density. The JWL coefficients A, B, R_1, R_2, ω and the reference density ρ_0 have been chosen for the product gases of the explosive PBX-9404 [21].

In Fig. 3, we illustrate the results of this Cartesian shock tube calculation by comparing the computed solution with the exact solution. The latter was obtained with the exact Riemann problem solver described in Section 1. There are 180 zones in the computational domain, with the initial discontinuity located between zones 60 and 61. These materials are modeled by the JWL and Gilmore EOS routines. The initial data were $(\rho_L, e_L, u_L) = (2.0, 6.0 \times 10^{11}, 0.0)$ and $(\rho_R, e_R, u_R) = (1.2913 \times 10^{-3}, 2.0 \times 10^9, 0.0)$. Here and in the figures, all quantities are in cgs units.
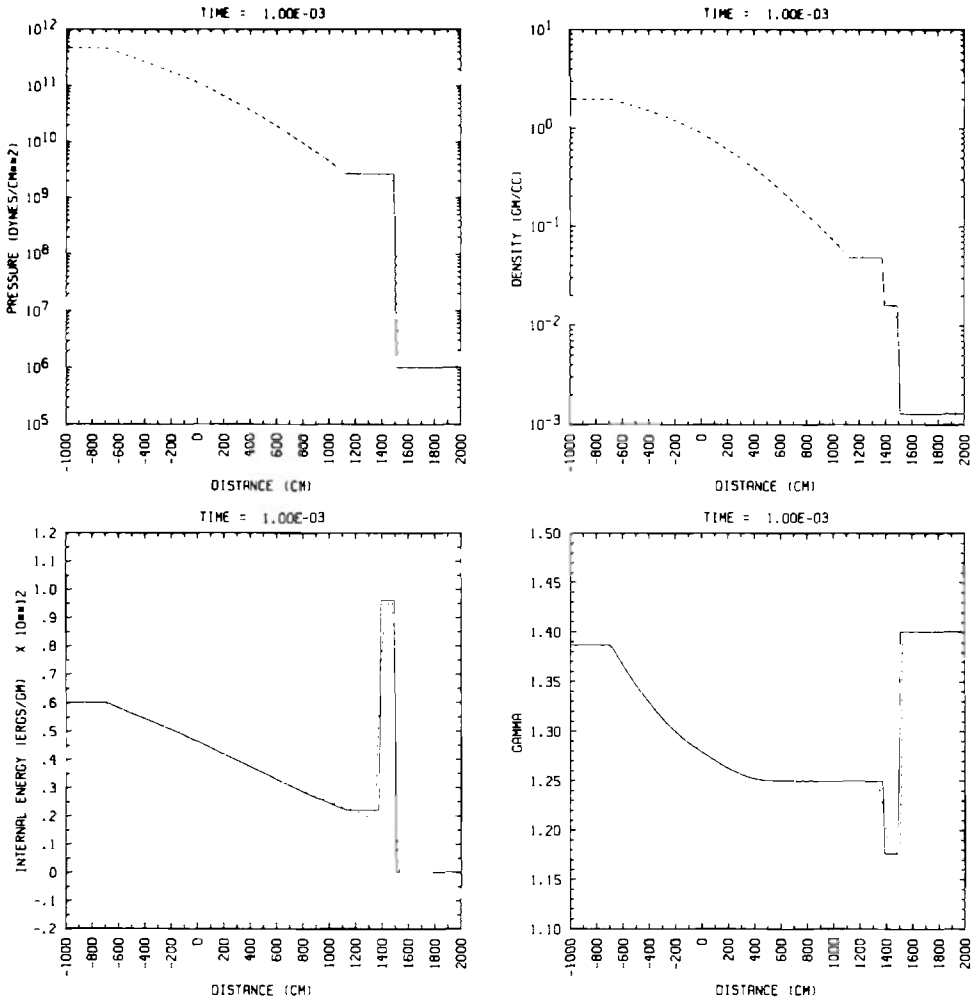
FIG. 3. Solution for a Cartesian shock tube with explosive product gases on the left and atmospheric air on the right. The solid line is the exact solution, computed using the algorithm in Section 1; the dashed line is the solution computed using the Eulerian second order Godunov method with 180 zones. The quantities plotted are pressure, density, internal energy, and γ.

The boundary between the two materials is "tracked" by solving an additional advection equation for the fraction of air in a zone. If the fraction is not 0 or 1, we take γ_j, Γ_j in a zone to be a weighted average, γ_{av}, Γ_{av}, of these quantities for each of the two materials. The pressure is then computed using the formula $p = (\gamma_{av} - 1)\rho e$. The computed solution is in good agreement with the exact solution. The slight undershoot in the internal energy to the left of the contact discontinuity is a starting error, which occupies a fixed number of zones as the mesh is refined. The density, energy, and pressure profiles are all monotone across the shock.
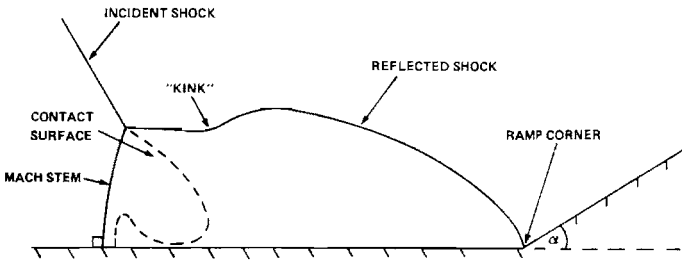
FIG. 4. Planar shock wave diffraction. The case illustrated is complex Mach reflection.

Our second test problem is a two-dimensional calculation of the reflection of a planar shock by an oblique surface, illustrated schematically in Fig. 4. Setting the origin of coordinates at the corner and measuring time with respect to the arrival of the incident shock at the corner, the solution for $t > 0$ is a function of $(x/t, y/t)$. This solution depends on the parameters $\alpha = $ ramp angle, $M_s = $ incident shock Mach number, and the equation of state of the fluid. This problem is well-known and has generated a great deal of analytical, experimental, and computational work in the last forty years; for a review of the experimental work in this area, see [16]. We consider here the case of a Mach reflection in air, with $\alpha = 20°$, $M_s = 7.19$. The ambient air for this experiment was $(\rho_0, p_0) = (9.29 \times 10^{-5}, 8.0 \times 10^4)$. Due to the low ambient pressure (less than 8 percent of atmospheric pressure) the results are sensitive to the correct representation of the equation of state; it is for this reason that we chose this particular problem as a test.

For real air, we consider three different equations of state: (1) a perfect gas with $\gamma = 1.4$, (2) the Gilmore real air EOS [10], and (3) the Hansen real air EOS [15]. Both the Gilmore and Hansen EOS routines are based on a detailed analysis of the statistical mechanics and kinetic theory of the constituents of air at high temperatures. The Hansen EOS is based on the analysis of [15] with some modification, described in [16]. The Gilmore EOS is specifically designed for efficiently computing the propagation of blast waves into atmospheric ambient conditions and is less valid for low density ambients, while the Hansen EOS is accurate at the low densities typical of shock tube studies. Each of these routines has been modified into a vectorized table lookup format. Table entries for γ and Γ are stored in arrays; at each EOS evaluation, linear interpolation between tabulated values is used.

Figure 5 is a photograph of an infinite fringe interferogram of this experiment, first published in [8]. The boundaries between the light and dark bands are isopycnics, i.e., lines of constant density. The density jump between successive bands is a constant. The experimental results contain physical phenomena which are not modeled by the Euler equations. The principal effect is due to vibrational non-equilibrium [23]. The Euler equations are valid under the assumption that all the thermodynamic degrees of freedom relax to equilibrium instantaneously behind shock waves. For the range of ambient conditions and shock Mach numbers considered in [8], this is true for the translational and rotational degrees of freedom of
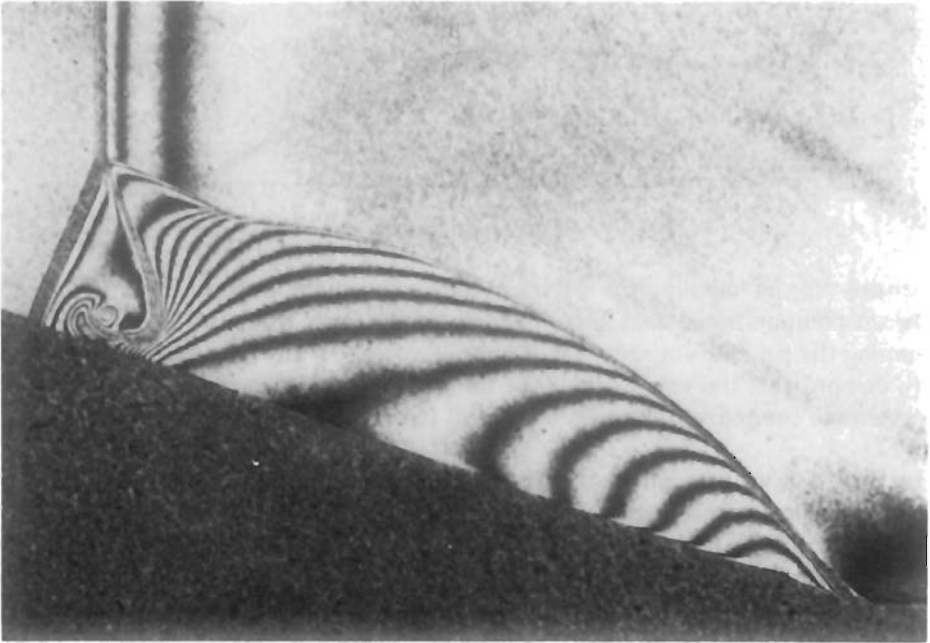
FIG. 5. Experimental isopycnics for complex Mach reflection, $\alpha = 20°$, $M_s = 7.19$. Reproduced, by permission of the publisher, and the authors, from [8, p. 39].

the gas, but not always for the vibrational degrees of freedom [23, 16]; in particular, the vibrational degrees of freedom for the example given here relax on time scales comparable to the hydrodynamic time scales. This is seen in the experimental results by the presence of isopycnics behind the incident shock, indicating the zone over which the gas relaxes to complete equilibrium. The curvature in the isopycnics under the reflected shock near the compression corner is also indicative of a relaxation zone. The effect of vibrational nonequilibrium on the density field is relatively small (about 10% of the shock jumps) and confined to relatively narrow bands near the shocks. Since our computational results are approximate solutions to the Euler equations, the assumption is being made that the gas relaxes instan-
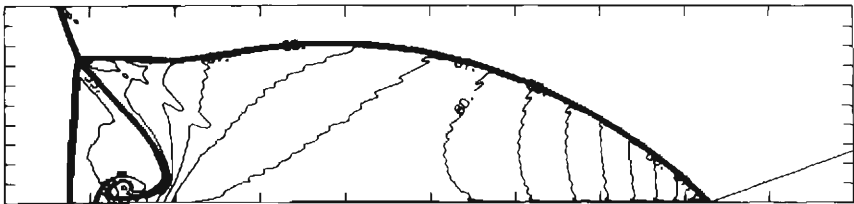

FIG. 6. Computed isopycnics for complex Mach reflection, $\alpha = 20°$, $M_s = 7.19$, using a polytropic EOS with $\gamma = 1.4$. The calculation was performed on a 510×120 grid consisting of square zones of length $\frac{1}{15}$ cm.
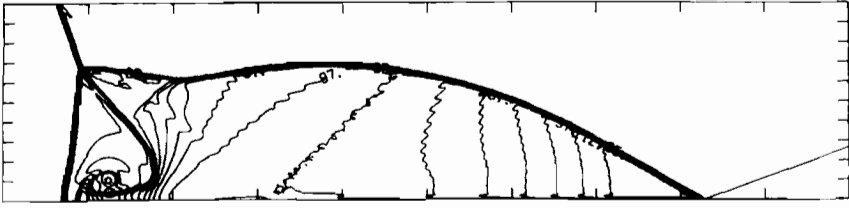
FIG. 7.   Same as Fig. 6, using the Hansen EOS.

taneously to its equilibrium values. Thus, one might expect good agreement between computational and experimental results away from the relaxation zone, assuming the equilibrium equation of state is correct. In any case, our main purpose is to demonstrate the sensitivity of the numerical solution to the equation of state; an extensive comparison between numerical results and the experiments will appear in [12].

In Figs. 6–8 we present the density contours from the numerical calculations of the shock reflection problem using the three equations of state. All the calculations obtain the same large scale structure which is also apparent in the experiment. There is a leading Mach triple point, with the reflected shock attached at the compression corner. Extending from the Mach triple point to the right is a slip surface, which, as it approaches the ramp, turns back toward the Mach stem to form a jet. The leading edge of this jet is Rayleigh–Taylor unstable, and has the charactristic rounded and blunt shape. There are, however, substantial differences in the detailed features of the three calculations. The length of the Mach stem, and the angles between the various discontinuities at the triple point, differ considerably. Also, the structure of the reflected shock for the $\gamma = 1.4$ case is considerably different from that for the other two cases. In the latter, the reflected shock near the compression corner is a straight line, separating two constant states. There is also a discontinuity in the derivative of the path of the reflected shock, forming a second Mach triple point. In the $\gamma = 1.4$ results, the reflected shock is curved all the way to the compression corner, and a second Mach configuration does not form, the nonconvex portion of the reflected shock remaining smooth. Finally, we see considerable differences in the jet. The jet becomes longer, and the density contours become more numerous and complicated, going from $\gamma = 1.4$ to the Hansen EOS to the Gilmore
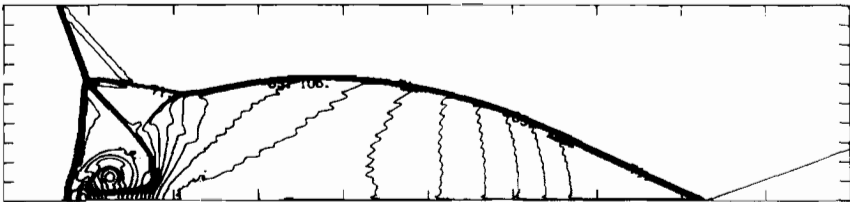

FIG. 8.   Same as Fig. 6, using the Gilmore EOS.

EOS. This is due to the increasing acceleration of the jet as a function of the equation of state. In the case of the Gilmore EOS results, there is an additional effect, which is the bulging, or "toeing out" of the Mach stem near the wall as it is pushed forward by the jet.

In Fig. 9, we give a more quantitative comparison between the various numerical results and the experimental data, by plotting the density at the wall as a function of the distance along the wall. We denote by x the distance along the wedge surface from the Mach stem, and L the distance from the Mach stem to the corner. The values of the density plotted for $x/L > 1$ are the values of the density behind the compression corner, and are equal to the density behind the incident shock. As one can see, there are large differences in the results for the three numerical calculations. This is due to the increasing compressibility of the fluid, going from $\gamma = 1.4$ to the Hansen EOS to the Gilmore EOS. The differences are largest in back of the leading edge of the jet, since the fluid has been compressed by two shocks, with the compression being the product of the compression due to each of the shocks. All of the numrical calculations show a small hot spot at $x/L \approx 0.4$. This is a numerical error, generated initially at the point where the incident shock intersects the upper boundary, and which propagates down into the interior of the solution. It is caused by the mismatch between the discrete travelling wave structure of the numerical incident shock and the analytic discrete shock used as a boundary condition. For a further discussion of this error, see [12, 24].
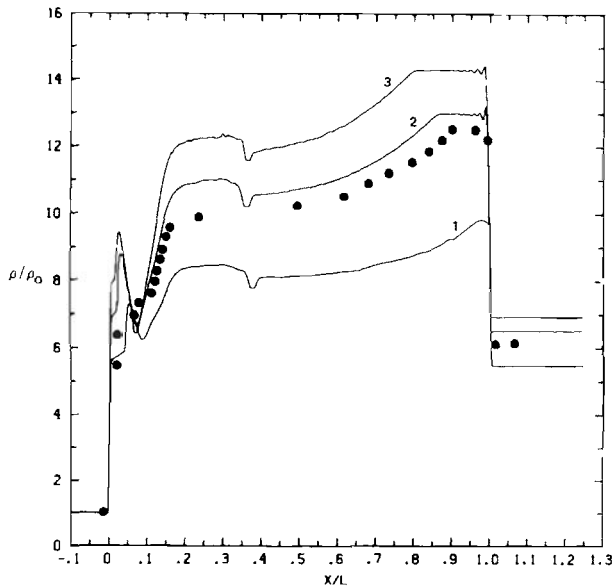

FIG. 9.   Density versus distance along the wall for the flowfields of Figs. 5–8; (1) polytropic EOS, (2) Hansen EOS, (3) Gilmore EOS. Solid dots—experimental data points taken from [8].

The comparison to the experiment in this case is complicated by the fact that the density cannot be completely determined from the experiment, since the number of isopycnics inside the shock cannot be resolved. Thus, it is necessary to make some assumption about the transition across the shock. The assumption made in [8] in interpreting the data was that the shock jumps adjacent to the ambient gas, as well as at the triple point, are given by the $\gamma = 1.4$ shock jump relations, even though the final equilibrium value of γ far downstream of the shock is not 1.4. Since the value of the density thus derived from the experimental data in the $x/L > 1$ region should be the equilibrium value (since it is well behind the relaxation zone), the difference between the computed density and the density derived from the experimental data is a measure of the incompatibility of the various equations of state with the assumptions made in deriving the experimental values of the density. For the correct equation of state, shifting the data by the fixed amount required to obtain agreement in the $x/L > 1$ region should bring the numerical results into very close agreement with the experiment [12]. This is indeed the case for the Hansen EOS: most of the density profile is within 2–3% of the experimental results if this shift of the data is performed. The main disagreement is near the leading edge of the jet, where there are substantial viscous effects, as evidenced by the fact that the experimental isopycnics intersect the wall at an oblique angle. In contrast, the data from the other two equations of state disagree with the experimental results by substantial percentages, even after the data is shifted.

4. DISCUSSION AND CONCLUSIONS

The use of numerical calculations for compressible flow problems arising in physics and engineering applications often requires the ability to calculate solutions for fluids having a general equation of state. Our results for planar shock diffraction illustrate this need by demonstrating that substantial EOS effects are present for flowfields with complicated wave interactions. The equation of state not only affects detailed quantitative properties such as the jump conditions, triple point trajectory, and the precise values for the isopycnics, but also the qualitative behavior of the important structures in the flowfield. We refer especially to the dynamics of the jet behind the Mach stem. A question which remains open concerning the shock wave diffraction calculations is the extent to which nonequilibrium effects cause the experimental and calculated flowfields to differ, even after the data reduction has been calibrated from the equilibrium equation of state. This issue will be discussed further in [12]. An obvious resolution to this problem would be the generalization of the second order Godunov scheme used here to treat the thermodynamic degrees of freedom which relax to equilibrium on time scales comparable to the hydrodynamic time scales with the appropriate rate equation [23].

To assess the relative costs of the various changes we have made in the second order Godunov algorithms to accommodate the general equation of state, we performed a series of timing comparisons, using as the test problem the one-dimen-

sional shock tube problem discussed in the previous section. The timings were performed on the Cray 1 at the Magnetic Fusion Energy Computer Center, with the programs compiled using the CFT compiler. We considered four cases:

(1) the algorithm implemented as in Section 2;

(2) the same program as for (1), but with the EOS call replaced by a dummy call which set $\gamma_j = \Gamma_j = 1.4$;

(3) the same program as for (2), but with the Riemann problem solution algorithm given in Section 2 replaced by the constant γ algorithm given in [2];

(4) the same program as for (3), but with the interpolation and characteristic calculations given by (47) omitted.

The times are given in the table below, in microseconds per zone per time step. The programs were vectorized in such a way that the results are independent of the initial data, and depend only on the number of mesh points in the calculation.

Cray 1	Timing Results
Case 1	24.2 μsec
Case 2	18.2 μsec
Case 3	14.2 μsec
Case 4	12.8 μsec

Thus, the difference in the time used between the real gas algorithm, excluding the call to the equation of state, and the polytropic algorithm, is 5.4 μsec (= (case 2) − (case 4)), about a 40% increase. Most of this increase is in the Riemann problem solver. A major source of this overhead is the necessity of guarding against zero denominators in the formulas for W^2 in (34), and in the secant iteration (18). Nonetheless, this increase is still smaller than the time required to perform the single EOS evaluation.

To generalize Godunov-type schemes originally designed for polytropic gases to the case of a general EOS, one must confront a number of issues. The principal one is the avoidance of numerous equation of state calls in the course of solving the Riemann problem. A related issue is the formulation of an algorithm which requires as little detailed information about the equation of state as possible. For example, an algorithm such as the one described in [18], which requires integration along the isentrope, could be quite expensive (see, e.g., [11]); furthermore, if the sound speed is obtained by numerically differentiating a tabulated pressure function using (5), instabilities might arise in regions where the table is sparse. We feel that we have successfuly dealt with these issues. In particular, the sound speeds in the Gilmore EOS were obtained by numerically differentiating tabulated values of pressure, and we obtained the same stability and robustness in the calculations performed with this EOS as those performed using the Hansen EOS, in which the sound speeds were obtained analytically. One area which we have not explored

thoroughly is the applicability of this method for fluids in which γ varies strongly at shocks. We have done some experiments calculating shock propagation in compressible water, in cases where there is an order of magnitude jump in γ across the shock, and have obtained results of comparable quality as those obtained for gases. We feel that the limiting of γ given by (32) is critical to the success of the algorithm in these regimes. For a strong shock wave, this guarantees that γ remains between the pre- and postshock values. We intend to explore the applicability of this method to high γ materials in future work.

ACKNOWLEDGMENTS

REFERENCES

1. A. J. CHORIN, *J. Comput. Phys.* **22** (1976), 517.
2. P. COLELLA, *SIAM J. Sci. Stat. Comput.* **3** (1982), 76.
3. P. COLELLA, *SIAM J. Sci. Stat. Comput.* **6** (1985), 104.
4. P. COLELLA, "Approximate Solution of the Riemann Problem for Real Gases," Lawrence Berkeley Lab. Rep. LBL-14442, 1982.
5. P. COLELLA AND H. M. GLAZ, Numerical modelling of inviscid shocked flows of real gases, *in* "Proceedings, Eighth International Conference on Numerical Methods in Fluid Dynamics, Aachen, 1982" (E. Krause, Ed.), Springer-Verlag, Berlin.
6. P. COLELLA AND P. R. WOODWARD, *J. Comput. Phys.* **54** (1984), 174.
7. R. COURANT AND K. O. FRIEDRICHS, "Supersonic Flow and Shock Waves," Interscience, New York, 1948.
8. R. L. DESCHAMBAULT AND I. I. GLASS, *J. Fluid Mech.* **131** (1983), 27.
9. B. M. DOBRATZ (Ed.), "Properties of Chemical Explosives and Explosive Simulants," Lawrence Livermore Lab. Rep. UCRL-51319, Dec. 15, 1972.
10. F. R. GILMORE, "Equilibrium Composition and Thermodynamic Properties of Air to 24,000 K," Rand Corp., RM-1543, 1955.
11. H. M. GLAZ, "Development of Random Choice Numerical Methods for Blast Wave Problems," Naval Surface Weapons Center Tech. Rep. NSWC/WOL TR 78-211, March 1979.
12. H. M. GLAZ, P. COLELLA, I. I. GLASS, R. L. DESCHAMBAULT, "A Numerical Study of Oblique Shock Reflections, with Experimental Comparisons," *Proc. R. Soc. Lond. B*, in press.
13. H. M. GLAZ AND A. B. WARDLAW, *J. Comput. Phys.*, expected to appear prior to this paper.
14. S. K. GODUNOV, *Mat. Sb.* **47** (1959), 271. [in Russian]
15. C. F. HANSEN, "Approximations for the Thermodynamic and Transport Properties of High-Temperature Air," NASA TR R-50, 1959.
16. J.-H. LEE AND I. I. GLASS, "Domains and Boundaries of Pseudo-stationary Oblique Shock-Wave Reflections in Air," University of Toronto Institute for Aerospace Studies Rep. 262, June 1982.
17. T.-P. LIU, *J. Differential Equations* **18** (1975), 218.
18. S. OSHER AND F. SOLOMON, *Math. Comput.* **38** (1982), 339.

19. P. ROE, *J. Comput. Phys.* **43** (1981), 357.

20. R. G. SMITH, *Trans. Amer. Math. Soc.* **249** (1979), 1.

21. H. M. STERNBERG AND H. HURWITZ, Calculated spherical shock waves produced by condensed explosives in air and water, *in* "Sixth Symposium (International) on Detonation," Naval Surface Weapons Center, White Oak, August 24–27, 1971.

22. B. VAN LEER, *J. Comput. Phys.* **32** (1979), 101.

23. W. G. VINCENTI AND C. H. KRUGER, "Introduction to Physical Gas Dynamics," Krieger, Huntington, N.Y., 1975.

24. P. R. WOODWARD AND P. COLELLA, "Numerical simulation of two-dimensional fluid flow with strong shocks," *J. Comput. Phys.* **54** (1984), 115.